





Article

Additive Manufacturing of Compositionally-Graded AISI 316L to CoCrMo Structures by Directed Energy Deposition

Niklas Sommer ^{1,*}, Philipp Kluge ², Florian Stredak ¹, Sascha Eigler ¹, Horst Hill ², Thomas Niendorf ³
and Stefan Böhm ¹

- ¹ Department for Cutting and Joining Manufacturing Processes, Institute for Production Technologies and Logistics, University of Kassel, Kurt-Wolters-Straße 3, 34125 Kassel, Germany; uk007724@student.uni-kassel.de (F.S.); s.eigler@uni-kassel.de (S.E.); s.boehm@uni-kassel.de (S.B.)
- ² Deutsche Edelstahlwerke Specialty Steel GmbH & Co. KG, Special Materials, Oberschlesienstraße 16, 47807 Krefeld, Germany; Philipp.Kluge@DEW-STAHLCOM (P.K.); Horst.Hill@DEW-STAHLCOM (H.H.)
- ³ Institute of Materials Engineering—Metallic Alloys, University of Kassel, Mönchebergstraße 3, 34125 Kassel, Germany; niendorf@uni-kassel.de
- * Correspondence: n.sommer@uni-kassel.de

Abstract: In the present study, compositionally-graded structures of AISI 316L and CoCrMo alloy are manufactured by powder-based laser-beam directed energy deposition (DED-LB). Through a process-integrated adjustment of powder flow, in situ alloying of the two materials becomes feasible. Thus, a sharp and a smooth transition with a mixture of both alloys can be realized. In order to investigate the phase formation during in situ alloying, a simulation approach considering equilibrium calculations is employed. The findings reveal that a precise compositional as well as functional gradation of the two alloys is possible. Thereby, the chemical composition can be directly correlated with the specimen hardness. Moreover, phases, which are identified by equilibrium calculations, can also be observed experimentally using scanning electron microscopy (SEM) and energy-dispersive X-ray-spectroscopy (EDS). Electron backscatter diffraction (EBSD) reveals epitaxial grain growth across the sharp transition region with a pronounced <001>-texture, while the smooth transition acts as nucleus for the growth of new grains with <101>-orientation. In light of envisaged applications in the biomedical sector, the present investigation demonstrates the high potential of an AISI 316L/CoCrMo alloy material combination.

Keywords: additive manufacturing; directed energy deposition; compositionally-graded materials; functionally-graded materials; mechanical properties; microstructural evolution; computational material science



Citation: Sommer, N.; Kluge, P.; Stredak, F.; Eigler, S.; Hill, H.; Niendorf, T.; Böhm, S. Additive Manufacturing of Compositionally-Graded AISI 316L to CoCrMo Structures by Directed Energy Deposition. *Crystals* **2021**, *11*, 1043. <https://doi.org/10.3390/cryst11091043>

Academic Editor: Hongbin Bei

Received: 10 August 2021

Accepted: 26 August 2021

Published: 30 August 2021

Publisher's Note: MDPI stays neutral with regard to jurisdictional claims in published maps and institutional affiliations.



Copyright: © 2021 by the authors. Licensee MDPI, Basel, Switzerland. This article is an open access article distributed under the terms and conditions of the Creative Commons Attribution (CC BY) license (<https://creativecommons.org/licenses/by/4.0/>).

1. Introduction

Additive manufacturing (AM) is a novel manufacturing method that utilizes the layerwise deposition of material to produce parts from manifold materials, e.g., metals [1]. Two prominent AM processes with respect to the fabrication of metals are powder bed fusion (PBF) and directed energy deposition (DED) [2], of which the latter is also known as laser-engineered net-shaping (LENS) [1]. In comparison to PBF, where a heat source such as a laser or electron beam is used to achieve a localized melting of a powder bed, DED is characterized by the direct feed of powder- or wire-based material to the process zone, where it is melted by a focussed heat source, e.g., by a laser beam [1,2].

The aforementioned layerwise deposition of material enables unprecedented geometrical freedom and complexity during both, construction and fabrication [1]. Furthermore, the control of process parameters in PBF processes allows for tailored microstructures within a single component and, thus, adapting the mechanical properties to a specific application eventually opening pathways towards functionally-graded AM components [3–6]. In addition, DED allows for the use of multiple materials to be fed into the process zone subsequently and simultaneously, such that multi-material additive manufacturing (MMAM) is

enabled [7,8]. The continuous transition from one material to another facilitates resource efficient use of material in line with the specific application, and it also reduces the susceptibility to crack formation [9]. Moreover, DED can be used to tailor the components porosity, for example to increase the bond between an implant and its host tissue [10].

Thus, DED is very promising for the fabrication of multi-material, load-bearing implants with tailored chemical and structural properties [10–12]. In light of the envisaged application, alloys with excellent biocompatibility and in-vivo characteristics, such as Ti–6 Al–4 V or CoCrMo, were in focus of recent research [10–12]. In particular, CoCrMo-based alloys are characterized by superior properties as metal-on-metal hip-implants when compared to conventional implants [13]. The feasibility to manufacture implants of CoCrMo-based ASTM F75 alloy with patient-adapted geometry has further attracted the attention of research in PBF-based AM-processes, such as laser-based powder-bed-fusion (PBF-LB) [14–23] and electron-beam-based powder bed-fusion (PBF-EB) [24–26]. Until now, the immanent boundary conditions of PBF-processes only allow for a somewhat limited in situ change of chemical composition or local reinforcement, which is still the subject of recent research [27–29].

With the increasing worldwide demand for cobalt, which is expected to quadruple from 2017 to 2023 due to its use in lithium batteries [30], a resource-efficient application of cobalt-based CoCrMo alloy is necessary. Therefore, the use of laser-based DED to fabricate compositionally graded, multi-material combinations of CoCrMo is investigated in the present study. In order to enable and maintain fields of application within the biomedical sector, AISI 316L stainless steel is chosen as secondary material, which—to the best of the author’s knowledge—has not been published as compositionally-graded material in combination with a biomedical-grade CoCrMo alloy before. In order to evaluate the influence of the material transition on the microstructural evolution, crack formation, and mechanical properties, two different transition conditions are investigated: a sharp transition from AISI 316L to CoCrMo and a smooth transition with a 50 wt.% 316L and 50 wt.% CoCrMo zone layer between the two materials.

2. Materials and Methods

2.1. Powder Materials and Process Setup

As powder materials, CoCrMo (Printdur CoCrF75, Deutsche Edelstahlwerke Specialty Steel GmbH & Co. KG, Krefeld) and AISI 316L (Printdur 4404, Deutsche Edelstahlwerke Specialty Steel GmbH & Co. KG, Krefeld) with a nominal powder size distribution of 50–150 μm were used. The measured particle size distribution is shown in Figure 1, while the chemical composition is depicted in Table 1. As substrate material, plates of AISI 304 stainless steel with dimensions of 50 \times 50 \times 10 mm^3 were used.

Table 1. Chemical composition of the powder materials used in the investigation. In wt.%. AISI 316L also used in [31].

Alloy	C	Si	Mn	P	S	Cr	Mo	Ni	Fe	Co
AISI 316L	0.03	0.7	0.5	0.015	0.011	16.5	2.1	13.0	bal.	-
CoCrMo	0.05	0.9	0.9	-	-	27.2	8.2	-	0.3	bal.

The powder was fed to the processing optics using a two-disc powder feeder (GTV PF2/2, GTV Verschleißschutz GmbH, Luckenbach, Germany) using Argon carrier-gas (grade 4.6, purity $\geq 99.996\%$) with a flow rate of 10 L min^{-1} . A three-jet, coaxial powder nozzle (Fraunhofer ILT, Aachen, Germany) with a standoff distance of 12 mm was mounted to the processing optics (Reis Lasertec MWO44, KUKA Industries GmbH & Co. KG, Aachen, Germany) for AM. The feed motion was realized through a six-axis robot (Reis RV30-26, KUKA Industries GmbH & Co. KG, Obernburg, Germany). As beam source, a 2 kW fiber laser (IPG YLS-2000-S2, IPG Laser GmbH, Burbach, Germany) with a wavelength of 1070 nm and a top-hat intensity profile was used, whose beam was guided to the

processing optics using a fiber with a diameter of 400 μm . The utilization of a lens with a focal length of 300 mm yielded an approximate beam diameter of 1.2 mm on the workpiece. To prevent oxidation of the structures during manufacturing, Argon shielding gas (grade 4.6, purity $\geq 99.996\%$) with a flow rate of 10 L min^{-1} was fed through the coaxial outlet of the powder nozzle.

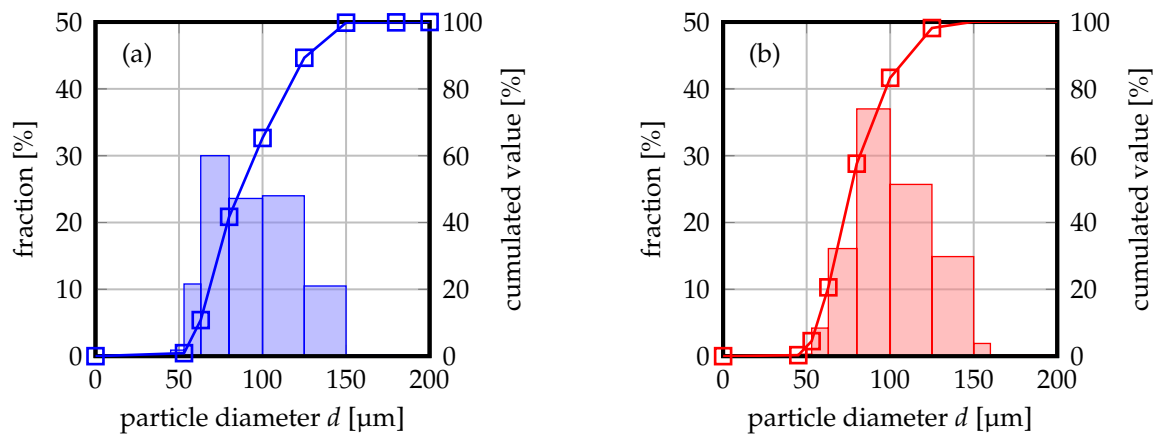


Figure 1. Particle size distribution of (a) AISI 316L and (b) CoCrMo powder material used in the experiments. (a) adopted from [31].

Thin-wall structures with dimensions of approximately $40 \times 40 \times 2 \text{ mm}^3$ were fabricated using a traverse speed of 600 mm min^{-1} and a bi-directional scanning strategy (Figure 2a,b). As the DED-LB system in the present investigation did not allow for the implementation of an adapted powder feed algorithm to prevent inhomogeneous material deposition, e.g., as reported by Calleja et al. [32], run-in and run-out lengths for a constant traverse motion were introduced (see detail in Figure 2a). To compare different transition conditions from AISI 316L to CoCrMo, smooth and sharp transitions were manufactured and analyzed. Based on the process-intrinsic capabilities of laser-based DED enabling in situ alloying, a transition zone consisting of 50 wt.% AISI 316L and 50 wt.% CoCrMo with an approximate height of 10 mm was added to the previously built AISI 316L layers for a smooth transition, while the sharp transition meant that CoCrMo was directly fabricated on top of the previous AISI 316L layers (Figure 2c,d). The powder feed rates applied during the process were 10 g min^{-1} and 12 g min^{-1} for AISI 316L and CoCrMo, respectively. The used powder feed rates were fixed based on preliminary investigations with respect to the clad geometry. Feed rates for the transition zone were adapted accordingly. Within the AISI 316L fabrication zone, a laser power of 900 W was employed, while it was reduced to 800 W for the zone of CoCrMo. The nozzle-standoff-distance was kept at a constant value of 12 mm, while the focal offset of the laser beam was set to 0 mm, which resulted in an overlap of powder and laser focus.

2.2. Microstructural Characterization and Mechanical Testing

After the build-up process, the generated structures were removed from the base-plate using a wet-cutting machine. To allow for characterization of the microstructure within the samples, polished and etched cross-sections were characterized using optical microscopy (OM; DM2600, Leica Microsystems GmbH, Wetzlar, Germany) and scanning electron microscopy (SEM; Zeiss REM Ultra Plus, Carl Zeiss Microscopy, Oberkochen, Germany). In order to analyze grain orientation, electron-backscatter diffraction (EBSD, Bruker e^- -flash) was employed. For EBSD measurements, the SEM was operated with an acceleration voltage of 20 kV. The chemical gradient within the samples was investigated using optical emission spectroscopy (OES; OBLF QSG/QSN750, OBLF Spektrometrie, Witten, Germany) and energy-dispersive X-ray spectroscopy (EDS; Zeiss EVO50, Carl Zeiss Microscopy, Oberkochen, Germany). For EDS-measurements, the SEM was operated at an

acceleration voltage of 15 kV. In order to obtain a sufficient spatial resolution during OES, five equidistant measurement points were set along the build direction of the samples.

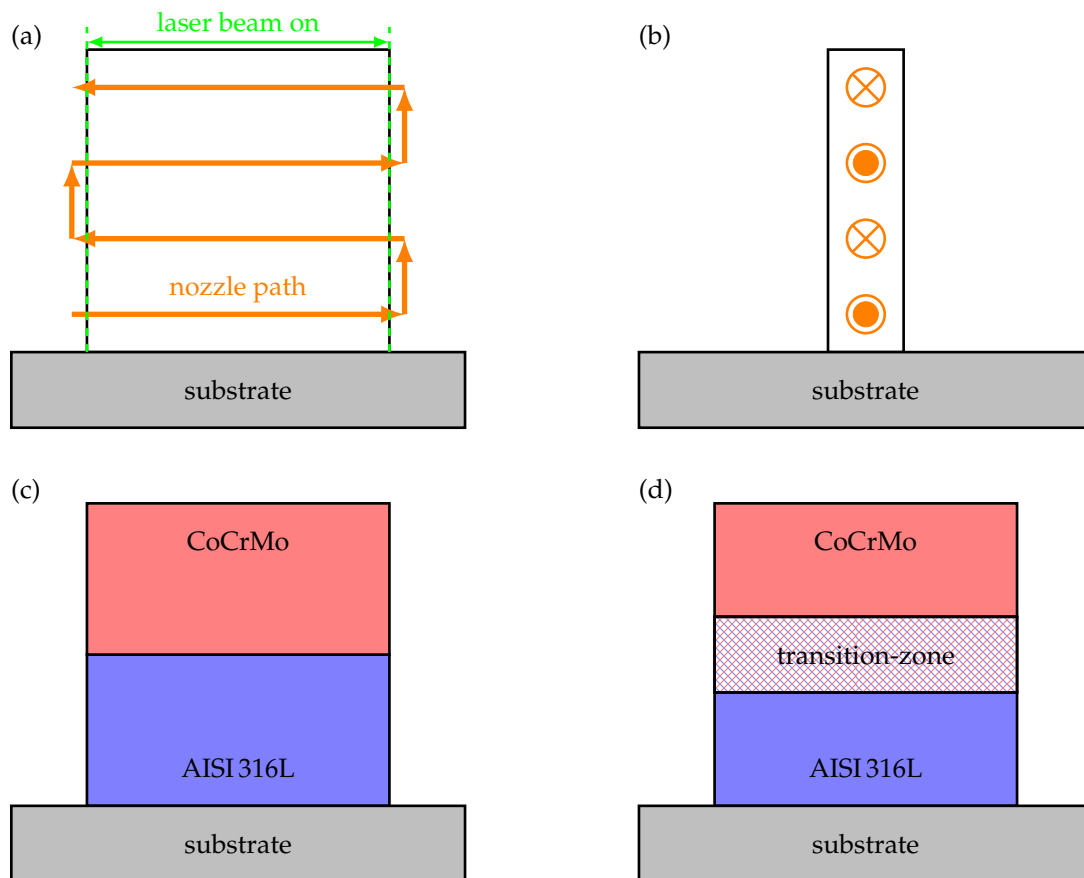


Figure 2. Schematic introducing the bi-directional scanning strategy and the different structures manufactured by laser-based DED, where arrows indicate the feed motion. (a) side view, (b) front view, (c) sharp transition, (d) smooth transition.

Prior to the microstructural characterization, samples were ground using SiC-paper and polished to 0.1 μm surface finish using colloidal SiO_2 . The 316L-based regions were etched using V2A-etchant (47.15% HCl, 47.15% H_2O , 4.7% HNO_3 , and 1% pickling inhibitor) for a duration of 30 s at room temperature, while the CoCrMo-based part was electrolytically etched with 60% perchloric acid (HClO_4) for 6 s at a voltage of 4 V. For EBSD-measurements, the samples were polished with diamond suspension of grit size 0.05 μm to achieve an optimal surface finish. Vickers hardness tests in accordance with standard HV0.1 (load 0.9807 N) were conducted using an automated hardness-testing machine (KB30, KB Prüftechnik GmbH, Hochdorf-Assenheim, Germany).

Subsequently, tensile specimens, whose geometry and location within the structures are depicted in Figure 3a,b, were extracted from the samples using electrical discharge machining (EDM) parallel to the build direction (BD). Before EDM, the surface of the structures was milled to achieve an improved surface finish and realize an overall thickness within the tensile testing specimens of 1.2 mm. Tensile tests were conducted using a tensile-testing machine (Z100, ZwickRoell AG, Ulm, Germany) in accordance to DIN EN ISO 6892-1 [33] with a strain rate of 0.0067 s^{-1} and a contactless extensometer.

2.3. Software and Simulation

To allow for characterization of stable phases within the compositionally-graded zones of the AM samples and a comparison with results obtained by microscopy, a computer-aided simulation approach was employed. For this purpose, the commercially available software *ThermoCalc* (version 2021a, v2021.1.79906-475) with the SSOL7 material database

was used to perform equilibrium calculations. As boundary condition, the chemical composition of the transition zones, which was experimentally determined using OES, was used. Additional boundary conditions with respect to ambient temperature and pressure were set to 293.15 K and 1 bar, respectively.

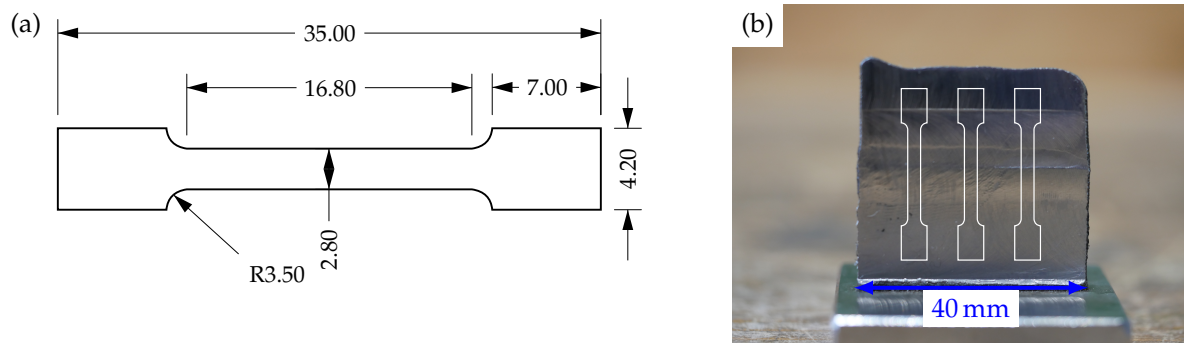


Figure 3. (a) Specimen geometry used for tensile testing, adopted from [34]. Dimensions in millimeter; (b) location of tensile testing specimens within the structures manufactured by laser-based DED. Depicted is as-milled surface condition.

3. Results and Discussion

In order to characterize the microstructural evolution of the two materials upon fabrication by DED-LB, etched cross-sections, which are depicted in Figure 4, were examined. As can be deduced from Figure 4a, the meltpool boundaries of fabricated layers in AISI 316L are visible in the etched micrograph. Moreover, no defects such as pores, cracks or zones with lack-of-fusion can be identified. The microstructure of AISI 316L is characterized by columnar grains, which are elongated in build direction. Furthermore, subgrain structures with different orientations can be distinguished as well. It should be noticed that the columnar grain growth of DED-316L is not suppressed by the meltpool boundaries. Rather, grains grow over the meltpool boundaries as a result of repeated remelting, and, thus, grain lengths being a multiple of grain widths can be observed. Similar results are obtained for DED-CoCrMo alloy, demonstrating large, columnar grains in BD as well (Figure 4b). The sample is also free of internal defects, eventually demonstrating that a robust fabrication of both materials is feasible.

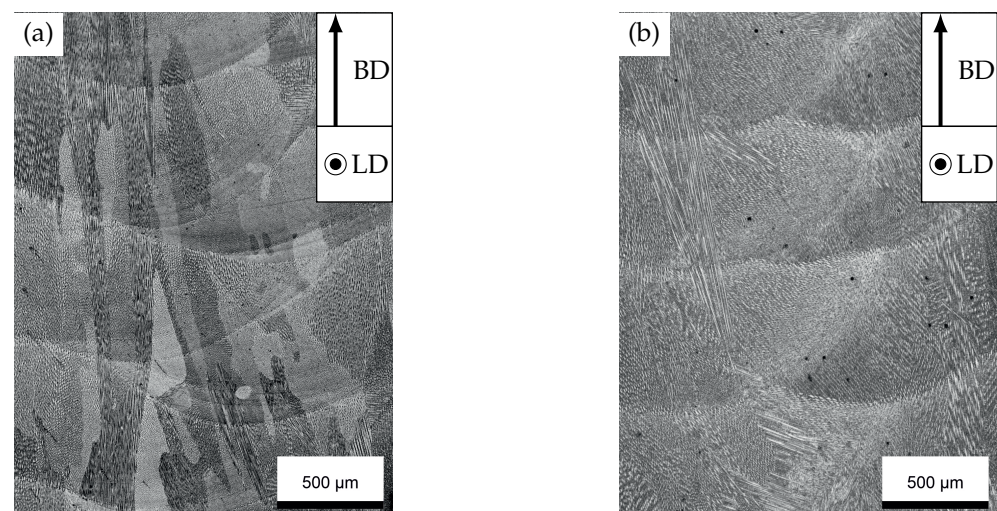


Figure 4. Etched micrographs detailing (a) AISI 316L and (b) CoCrMo microstructure in as-built condition, obtained by laser-based DED. BD is vertical.

The EBSD-analysis, which is shown in Figure 5, reveals the evolution of a pronounced $\langle 001 \rangle$ -texture in AISI 316L. In contrast, the DED-processed CoCrMo regions are character-

ized by only a weak texture. While the grains in the interior of the thin-wall-structures seem to solidify in $\langle 101 \rangle$ orientation, the grains at the outer edges of the structures are characterized by a $\langle 001 \rangle$ orientation. The evolution of a $\langle 001 \rangle$ -texture in face-centered-cubic (fcc) materials, such as AISI 316L, can be explained by epitaxial grain growth and has been documented for PBF-LB for example by Thijs et al. [3] as well as Niendorf et al. [4]. While Thijs et al. [3] found that large temperature gradients and comparatively small melt pool dimensions lead to fine grained microstructures, the results shown are rather in good agreement with the findings of Niendorf et al. [4], who proposed that the direction of heat flow determined the texture evolution in PBF-LB processes. By comparing those results to the DED-LB process in the present study, it is evident that the heat flow originating from the process can only dissipate through the thin-wall structure and its substrate, as the surrounding atmosphere acts as an insulator. Therefore, it can be concluded that in DED-LB of thin-wall structures, the texture evolution of the fcc-materials is clearly dependent on heat flow through the structure. Furthermore, the temperature gradient G and crystal growth rate R , which were presented as main influencing factors on weld microstructure by David and Vitek [35], have to be taken into account. The phase mappings of the two materials demonstrate a dominant fcc solidification, which was also found for other additively manufactured AISI 316L [4] and CoCrMo [20] specimens in the as-built condition. Obviously, the fcc \rightarrow hcp transformation during cooling of the cobalt-based alloy [36] is suppressed and, thus, a nearly complete fcc matrix is obtained.

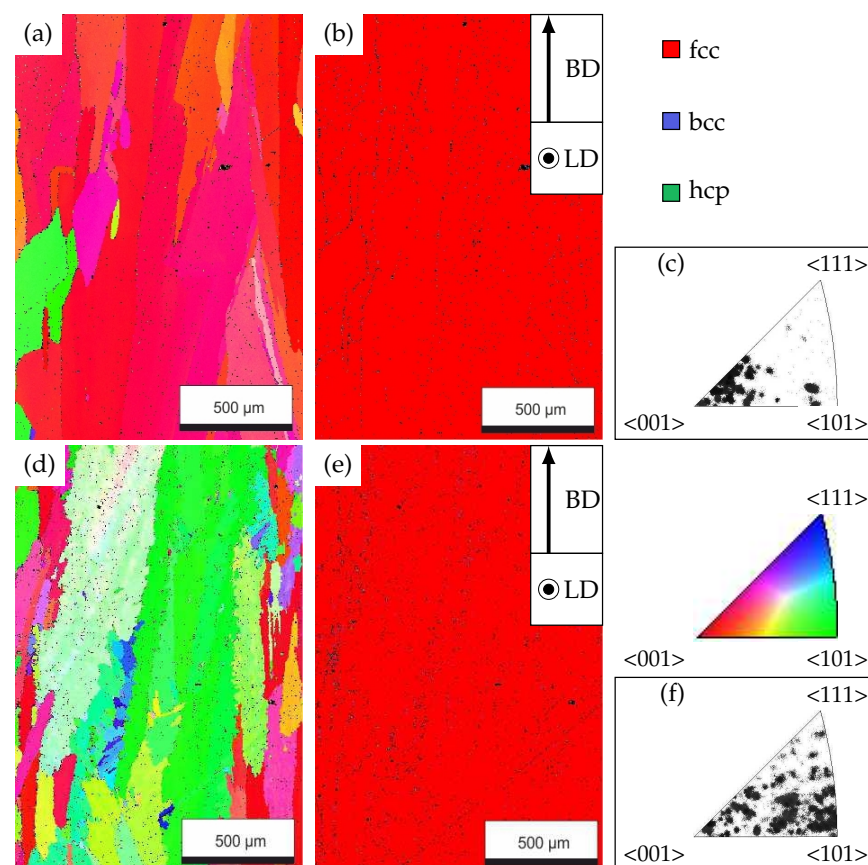


Figure 5. Inverse pole figure mappings (IPFM), phase mappings (PM), and inverse pole figures (IPF) of (a–c) pure AISI 316L and (d–f) pure CoCrMo zones. Grain orientations are plotted with respect to BD.

Since etching of the transition regions did not lead to satisfactory results due to the different chemical compositions involved, advanced measurement techniques were necessary to enable an in-depth characterization. First, OES measurements in the transition regions were conducted. As is depicted in Table 2a, the chemical composition of the transition regions varies significantly. While within the gradient sample, Co and Fe can be

found in almost equal distribution, the sharp transition is characterized by a composition of 51.3 wt.% Co and only 13.4 wt.% Fe. The latter may be attributed to the positioning-accuracy of the OES system, eventually indicating a measurement closer to the regions of CoCrMo. However, the results shown indicate an almost equal distribution between Co and Fe and, thus, undergird the successful in situ chemical gradation of the samples to the desired composition by DED-LB.

Obviously, the compositional gradation of the two materials involved leads to new alloy systems, whose properties may not be fully described in the literature. Thus, the authors decided to include results obtained by a combined simulation approach to predict a possible equilibrium phase composition based on the chemical compositions identified by OES. The results, which are depicted in Table 2b, demonstrate the formation of body-centered-cubic (bcc) phases in both sharp and smooth transition regions. Additionally, the equilibrium phase of the sharp transition is characterized by some hexagonal-closest-packed (hcp) phase, which may be explained by the higher Co-content identified in the OES analysis and its inherent fcc→hcp phase transformation [20]. In addition, carbide precipitates of the $M_{23}C_6$ type and M_6C type can be identified through computational analysis in sharp and smooth transition zones, respectively. Furthermore, the computational phase analysis of both transition regions shows the formation of Cr-, Mo- and Si-based intermetallics of different stoichiometry. Here it is important to note that these computational phase calculations are based on equilibrium assumptions, which may not be valid in DED-LB due to its inherent solidification and cooling characteristics. Thus, the findings of the thermodynamic simulation have to be carefully compared to those obtained by SEM imaging and EDS measuring techniques.

Table 2. (a) Chemical composition of the transition zones of MMAM samples of AISI 316L and CoCrMo determined by OES, in wt.%. (b) Computational phase composition based on equilibrium calculations in *ThermoCalc*.

(a)								
Transition	Chemical Composition							
	C	Si	Mn	Cr	Mo	Ni	Co	Fe
sharp	0.01	0.82	0.72	24.9	6.58	2.02	51.3	13.4
smooth	0.01	0.67	0.62	22.00	4.60	5.32	32.29	34.29
(b)								
Transition	Phases							
	bcc	hcp	Co_3Mo	Cr_3Si	$M_{23}C_6$	Ni_5Si_2		
sharp	bcc	hcp	Co_3Mo	Cr_3Si	$M_{23}C_6$	Ni_5Si_2		
smooth	bcc	CrNi	M_6C	Mo_3Si	Ni_5Si_2			

The SEM-images of the two transition regions and corresponding EDS-measurement points are depicted in Figure 6a,b. Within each transition region, four EDS-spectra were measured, whose results are depicted in Figure 6c. From the results of the SEM images, it is evident that the microstructural features within the sharp and smooth transition zones show some similarities. In both transition zones, areas being characterized by material segregation are visible in the SEM images. These segregations can also be verified by EDS measurements (A1 → A2 and B1 → B3 in Figure 6). In light of the fact that these segregations can be observed in both sharp and smooth transition zones, they do not seem to be caused by the compositional adjustment within these zones but rather the melt pool dynamics and solidification characteristics of the DED-process. In addition to these solid-solution phases, precipitates can be identified within both transition regions. The most prominent precipitate feature of the two transition zones is a needle-shaped precipitate being rich in molybdenum and chromium when compared to the surrounding crystal (A3 and B4 in Figure 6). Within the smooth transition region, similar precipitates can also be found below the needle-shaped precipitate in a rather rectangular shape. Deduced

from the shape and chemical composition of the precipitates, it can be assumed that these are mixed carbides, presumably of type M_6C or $M_{23}C_6$ —both of which were also identified in the thermodynamic simulation. Furthermore, within both transition regions, round precipitates of different diameters can be seen. Taking the chemical composition of the latter into consideration (A4 in Figure 6), it can be perceived that these precipitates consist of oxygen, silicon, manganese, chromium, and aluminum. While the formation of some Si-containing intermetallics or precipitates can be expected based on the equilibrium calculations, none of these match the chemical composition of those identified within the transition region. However, this observation can be seen to be in good agreement with the findings of Tonelli et al. [23], who identified Si-rich particles of similar shape and composition in a CoCrMo alloy processed by PBF-LB. Therefore, the experimental findings obtained in both transition zones support some of the predictions and findings of the equilibrium calculations. However, it appears to be obvious that none of the bcc or hcp phases could be detected, as it is likely that the rapid solidification and cooling kinetics of the DED-LB process suppressed such transformations.

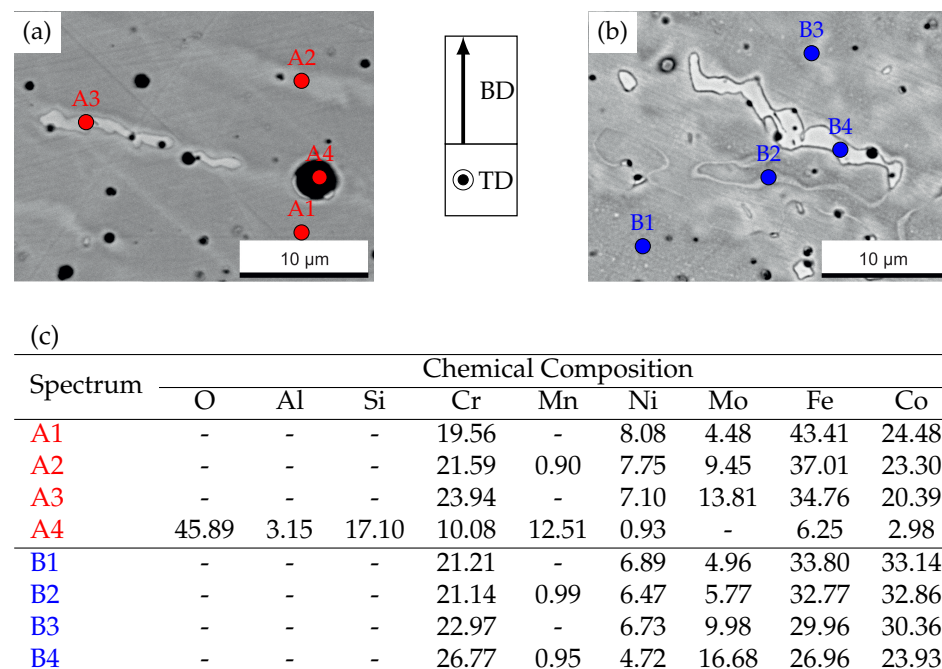


Figure 6. SEM-images of (a) sharp; (b) smooth transition zones of AISI316L and CoCrMo, with markers indicating locations of EDS-spectra measurements; (c) chemical composition based on obtained EDS-spectra, in wt.%.

In addition to the aforementioned differences in chemical composition, it was investigated if these variations had an influence on grain growth and grain orientation within the transition regions. An EBSD analysis of both transition regions was carried out, whose results are depicted in Figure 7. As can be derived from the sharp transition region in Figure 7a, the growth of columnar grains from AISI 316L across the boundary layer is somewhat limited, yet not fully suppressed. Interestingly, the grains that grow across the boundary mostly feature a $\langle 001 \rangle$ -orientation, which likely originates from the 316L material and its inherent solidification characteristics. In contrast, the in situ change in chemical composition within the smooth transition region (Figure 7c) demonstrates a strong influence on grain growth and grain orientation (notice the different scale bar). As can be deduced from EBSD analysis, the growth of grains from AISI 316L is suppressed. Rather, the change in chemical composition acts as nucleation point for the growth of large, $\langle 101 \rangle$ -oriented grains, which then continue their growth in build direction towards the regions of full-CoCrMo. The findings presented indicate that, in a sharp transition region, some of the $\langle 001 \rangle$ grain orientations of the parent material are adopted by the deposited

material on top as a result of epitaxial grain growth during solidification. However, some grains within the transition region grow with a $\langle 101 \rangle$ orientation based on nuclei being present in the transition region. A region of compositional gradation, on the other hand, acts as nucleus for the growth of grains with distinctively different orientations, in this case $\langle 101 \rangle$. Therefore, it can be derived that the in situ alloying may not only affect the chemical composition, but also grain growth and grain orientation. As both transition regions solidify in an fcc-lattice (Figure 7b,d), it is unknown why the grain orientation within Co-containing regions changes immediately. Obviously, further research using advanced diffraction methods is required to clarify these characteristics.

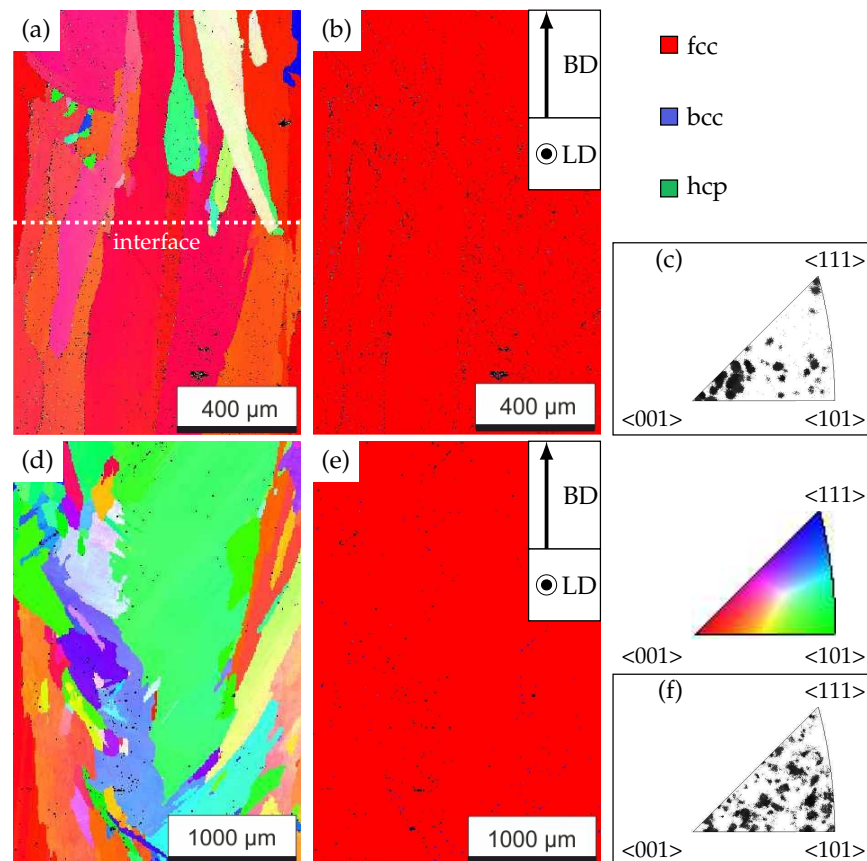


Figure 7. Inverse pole figure mappings (IPFM), phase mappings (PM) and inverse pole figures (IPF) of (a–c) sharp and (d–f) smooth transition regions. Grain orientations plotted with respect to BD.

Based on the differences in chemical composition, segregation zones and phase formation of the two transition regions, it was assessed if these differences had an influence on the mechanical properties. Hardness measurements were carried out and correlated with the results of OES-analysis along the build direction of the structures. Moreover, tensile tests in build direction were used to investigate whether the characteristic phase formation of the transition zones promotes a brittle and premature failure.

As can be derived from Figure 8a, the OES analysis and hardness mapping in BD confirm the successful establishment of a sharp transition. As expected, Iron, Chromium, and Nickel are the dominant elements found in the region of AISI 316L close to the substrate surface. This corresponds very well to a hardness of around 200 HV. However, the hardness changes rapidly in the sharp transition zone. In the transition zone, the Iron and Nickel contents are reduced rapidly, while, on the other hand, the content of Cobalt is increased drastically to over 50 wt.%. As the powder feed of AISI 316L had been stopped at this point, the residual fractions of iron and nickel can be attributed to the remelting of previous AISI 316L layers while depositing CoCrMo. Within this region, the hardness of the structures is increased from around 200 HV to more than 450 HV due to the chemical

gradient. The region of CoCrMo, which is characterized by comparatively high contents of cobalt, chromium and molybdenum, shows a hardness of approximately 500 HV. The results of the smooth transition zone, which are depicted in Figure 8b, reveal a slightly different behavior. While the chemical compositions measured by OES in the full-AISI 316L and full-CoCrMo are in good agreement with the results of the sharp transition specimen, the transition region is characterized by a smooth change in composition. At a sample height of 17.5 mm, an equal distribution between iron and cobalt, the two main elements of their respective alloys, is seen. Furthermore, the chemical composition with respect to chromium, molybdenum, and nickel corresponds very well to the desired composition of 50 wt.% AISI 316L and 50 wt.% CoCrMo. Moreover, the hardness mapping verifies the successful creation of not only a chemical, but also a mechanical gradient within the samples as the hardness in this region can be tailored to around 300 HV.

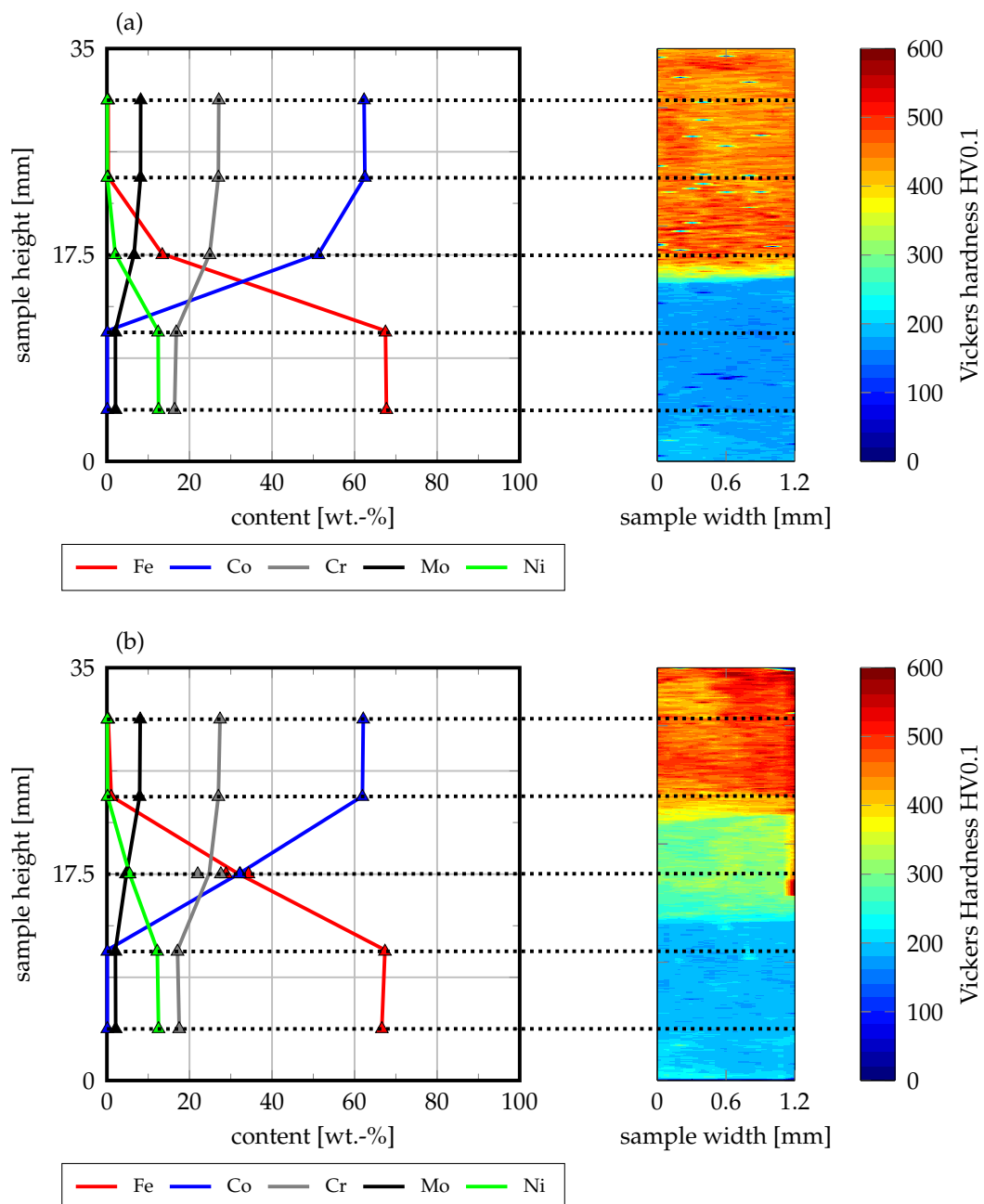


Figure 8. Correlation between chemical composition, analyzed by OES, and hardness distribution across the cross-section of AISI 316L/CoCrMo multi-material structures. (a) sharp transition, (b) smooth transition.

The results of tensile tests parallel to the build direction, which are presented in Figure 9, demonstrate a similar behavior for both, sharp and smooth transition specimens. The ultimate failure of the specimens is exclusively found within the regions of AISI 316L. Obviously, this can be attributed to the ultimate tensile strength (UTS) of AM-AISI 316L being lower than the UTS of AM-CoCrMo alloy [4,16]. Thus, plastic deformation is first initiated in this region and eventually leads to failure. Therefore, the experimentally determined properties are in good agreement with the mechanical properties of pure-AISI316L fabricated by DED-LB, which were recently published by Alvarez et al. [37].

The results of the tensile tests provide for a proof that none of the segregation zones within sharp and smooth transition zones lead to embrittlement and premature failure of the system. Thus, it can be concluded that the two alloy systems exhibit excellent chemical compatibility. Therefore, pathways towards further research in the field are opened.

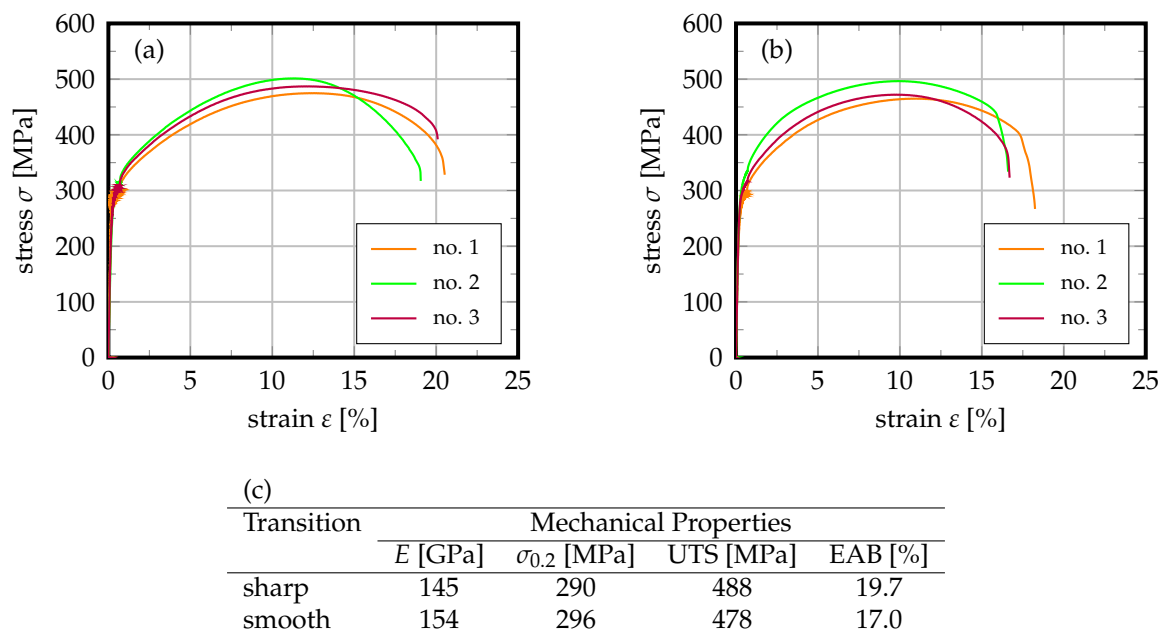


Figure 9. Results of tensile tests for specimens with (a) sharp and (b) smooth transition of AISI 316L and CoCrMo as well as (c) summary of mechanical properties, averaging three measurements for each transition.

4. Conclusions

In the present study, compositionally-graded structures of AISI 316L austenitic stainless steel and CoCrMo alloy were fabricated by powder-based DED-LB. In order to investigate the metallurgical compatibility, a sharp and smooth transition were created by in situ alloying. The findings demonstrate that powder-based DED-LB can be used to control and tailor the chemical composition of the manufactured parts with excellent precision, as the chemical composition of the gradient transition replicates the desired blend of 50 wt.% AISI316L and 50 wt.% CoCrMo. Moreover, the results of the chemical analysis for both, sharp and smooth transition, can be directly correlated with the hardness of the specimen; i.e., not only a chemical, but also a functional-mechanical gradation is achieved. In addition, tensile tests and SEM/EDS analysis verify that the two alloys exhibit excellent metallurgical compatibility. Eventually, they are not prone to embrittlement and premature failure. With respect to grain growth and grain orientation, elongated grains in build direction were identified for both transition conditions and regions. While the Fe-based regions are characterized by a strong $\langle 001 \rangle$ texture that is carried over the sharp transition, the smooth transition region acts as a nucleus for the growth of grains with pronounced $\langle 101 \rangle$ -orientation, which can also be found within the regions of the CoCrMo alloy. Moreover, some grains originating from the sharp transition region also feature a $\langle 101 \rangle$ -orientation despite a full fcc-lattice. Further research in the field is required in order

to clarify the characteristics of phase and texture evolution. Also, further investigations in the field will have to detail the corrosive properties of both transition regions as well as their in-vitro characteristics in order to open pathways towards an application in the biomedical sector. Heat treatments need to be carried out and characterized with regard to grain growth, texture, and inherent mechanical properties.

Author Contributions: Conceptualization, N.S.; methodology, N.S. and P.K.; validation, N.S., H.H., T.N. and S.B.; formal analysis, N.S. and P.K.; investigation, N.S., P.K., F.S. and S.E.; resources, P.K., H.H., T.N. and S.B.; data curation, N.S., P.K., F.S. and S.E.; writing—original draft preparation, N.S.; writing—review and editing, N.S., P.K., F.S., S.E., T.N. and S.B.; visualization, N.S.; supervision, H.H., T.N. and S.B.; project administration, N.S.; funding acquisition, S.B. All authors have read and agreed to the published version of the manuscript.

Funding: The research in the present investigation did not receive any additional funding.

Acknowledgments: The authors thankfully acknowledge the help of Michael Hübner during specimen extraction using EDM.

Conflicts of Interest: The authors declare no conflict of interest. The funders had no role in the design of the study; in the collection, analyses, or interpretation of data; in the writing of the manuscript; or in the decision to publish the results.

Abbreviations

The following abbreviations are used in this manuscript:

$\sigma_{0.2}$	yield strength
AM	additive manufacturing
AISI	American Iron and Steel Institute
ASTM	American Society for Testing and Materials
bcc	body-centered-cubic
BD	build direction
C	carbon
Co	cobalt
Cr	chromium
DED	directed energy deposition
DED-LB	laser-beam directed energy deposition
E	Young's modulus
EAB	elongation at break
EDM	electric discharge machining
EDS	energy-dispersive X-ray spectroscopy
fcc	face-centered-cubic
Fe	iron
H ₂ O	water
hcp	hexagonal-closest-packed
HCl	hydrochloric acid
HClO ₄	perchloric acid
HNO ₃	nitric acid
IQ	image quality
IPFM	inverse pole figure mapping
IPF	inverse pole figure
LENS	laser-engineered net-shaping
LD	longitudinal direction
Mn	manganese
Mo	molybdenum
MMAM	multi-material additive manufacturing
Ni	nickel
OM	optical microscopy
OES	optical emission spectroscopy
P	phosphorus

PM	phase mapping
PBF	powder bed fusion
PBF-EB	electron-beam powder bed fusion
PBF-LB	laser-beam powder bed fusion
S	sulfur
Si	silicon
SEM	scanning electron microscopy
TD	transversal direction
Ti	titanium
UTS	ultimate tensile strength
V	vanadium

References

- Gibson, I.; Rosen, D.; Stucker, B. *Additive Manufacturing Technologies: 3D Printing, Rapid Prototyping and Direct Digital Manufacturing*, 2nd ed.; Springer: New York, NY, USA; Heidelberg, Germany; Dodrecht, The Netherlands; London, UK, 2015.
- Deutsches Institut für Normung e. V. *Additive Manufacturing—General Principles—Terminology (ISO/ASTM DIS 52900:2018)*; German and English version prEN ISO/ASTM 52900:2018; Beuth Verlag GmbH: Berlin, Germany, 2018.
- Thijs, L.; Kempen, K.; Kruth, J.P.; van Humbeeck, J. Fine-structured aluminium products with controllable texture by selective laser melting of pre-alloyed AlSi10Mg powder. *Acta Mater.* **2013**, *61*, 1809–1819. [[CrossRef](#)]
- Niendorf, T.; Leuders, S.; Riemer, A.; Richard, H.A.; Tröster, T.; Schwarze, D. Highly Anisotropic Steel Processed by Selective Laser Melting. *Metall. Mater. Trans. B* **2013**, *44*, 794–796. [[CrossRef](#)]
- Niendorf, T.; Brenne, F.; Schaper, M.; Riemer, A.; Leuders, S.; Reimche, W.; Schwarze, D.; Maier, H.J. Labelling additively manufactured parts by microstructural gradation—Advanced copy-proof design. *Rapid Prototyp. J.* **2016**, *22*, 630–635. [[CrossRef](#)]
- Popovich, V.A.; Borisov, E.V.; Popovich, A.A.; Sufiiarov, V.; Masaylo, D.V.; Alzina, L. Functionally graded Inconel 718 processed by additive manufacturing: Crystallographic texture, anisotropy of microstructure and mechanical properties. *Mater. Des.* **2017**, *114*, 441–449. [[CrossRef](#)]
- Rodriguez, J.; Hofer, K.; Haelsig, A.; Mayr, P. Functionally Graded SS 316L to Ni-Based Structures Produced by 3D Plasma Metal Deposition. *Metals* **2019**, *9*, 620. [[CrossRef](#)]
- Zhang, C.; Chen, F.; Huang, Z.; Jia, M.; Chen, G.; Ye, Y.; Lin, Y.; Liu, W.; Chen, B.; Shen, Q.; et al. Additive manufacturing of functionally graded materials: A review. *Mater. Sci. Eng. A* **2019**, *764*, 138209. [[CrossRef](#)]
- Zou, H.; Chen, M.; Li, Y. Rapid manufacturing of FGM components by using electromagnetic compressed plasma deposition. In Proceedings of the International Conference on Intelligent Systems Research and Mechatronics Engineering (ISRME 2015); Zhengzhou, China, 11–13 April 2015; Liu, J., Wang, Y., Xu, H., Eds.; Advances in Intelligent Systems Research; Atlantis Press: Amsterdam, The Netherlands, 2015; [[CrossRef](#)]
- Bandyopadhyay, A.; Krishna, B.V.; Xue, W.; Bose, S. Application of laser engineered net shaping (LENS) to manufacture porous and functionally graded structures for load bearing implants. *J. Mater. Sci. Mater. Med.* **2009**, *20* (Suppl. 1), S29–34. [[CrossRef](#)]
- Vamsi, K.B.; Xue, W.; Bose, S.; Bandyopadhyay, A. Functionally graded Co-Cr-Mo coating on Ti-6Al-4V alloy structures. *Acta Biomater.* **2008**, *4*, 697–706. [[CrossRef](#)] [[PubMed](#)]
- Dittrick, S.; Balla, V.K.; Bose, S.; Bandyopadhyay, A. In vitro Wear Rate and Co Ion Release of Compositionally and Structurally Graded CoCrMo-Ti6Al4V Structures. *Mater. Sci. Eng. C Mater. Biol. Appl.* **2011**, *31*, 809–814. [[CrossRef](#)]
- Cuckler, J.M. The rationale for metal-on-metal total hip arthroplasty. *Clin. Orthop. Relat. Res.* **2005**, *441*, 132–136. [[CrossRef](#)]
- Facchini, L.; Magalini, E.; Robotti, P.; Molinari, A. Mechanical and microstructural characterization of astm f75 alloy produced by laser melting. *J. Biomech.* **2008**, *41*, S234. [[CrossRef](#)]
- Haan, J.; Asseln, M.; Zivcec, M.; Eschweiler, J.; Radermacher, R.; Broeckmann, C. Effect of subsequent Hot Isostatic Pressing on mechanical properties of ASTM F75 alloy produced by Selective Laser Melting. *Powder Metall.* **2015**, *58*, 161–165. [[CrossRef](#)]
- Mergulhão, M.V.; Podestá, C.E.; das Neves, M.D.M. Valuation of Mechanical Properties and Microstructural Characterization of ASTM F75 Co-Cr Alloy Obtained by Selective Laser Melting (SLM) and Casting Techniques. *Mater. Sci. Forum* **2017**, *899*, 323–328. [[CrossRef](#)]
- van Hooreweder, B.; Lietaert, K.; Neirinck, B.; Lippiatt, N.; Wevers, M. CoCr F75 scaffolds produced by additive manufacturing: Influence of chemical etching on powder removal and mechanical performance. *J. Mech. Behav. Biomed. Mater.* **2017**, *70*, 60–67. [[CrossRef](#)]
- Dikova, T. Bending fracture of Co-Cr dental bridges, produced by additive technologies: experimental investigation. *Procedia Struct. Integr.* **2018**, *13*, 461–468. [[CrossRef](#)]
- Song, C.; Zhang, M.; Yang, Y.; Di Wang; Jia-kuo, Y. Morphology and properties of CoCrMo parts fabricated by selective laser melting. *Mater. Sci. Eng. A* **2018**, *713*, 206–213. [[CrossRef](#)]
- Donkor, B.T.; Song, J.; Fu, Y.; Kattoura, M.; Mannava, S.R.; Steiner, M.A.; Vasudevan, V.K. Accelerated γ -face-centered cubic to ϵ -hexagonal close packed massive transformation in a laser powder bed fusion additively manufactured Co-29Cr-5Mo alloy. *Scr. Mater.* **2020**, *179*, 65–69. [[CrossRef](#)]

21. Omar, M.A.; Baharudin, B.T.H.T.; Sulaiman, S.; Ismail, M.I.S.; Omar, M.A. Characterisation of elemental analysis, carbon sulphur analysis and impact test of stent manufacturing using medical grade ASTM F75 cobalt chromium (CoCrMo) by selective laser melting (SLM) technology. *Adv. Mater. Process. Technol.* **2020**, *7*, 200–215. [[CrossRef](#)]
22. Sing, S.L.; Huang, S.; Yeong, W.Y. Effect of solution heat treatment on microstructure and mechanical properties of laser powder bed fusion produced cobalt-28chromium-6molybdenum. *Mater. Sci. Eng. A* **2020**, *769*, 138511. [[CrossRef](#)]
23. Tonelli, L.; Fortunato, A.; Ceschini, L. CoCr alloy processed by Selective Laser Melting (SLM): effect of Laser Energy Density on microstructure, surface morphology, and hardness. *J. Manuf. Process.* **2020**, *52*, 106–119. [[CrossRef](#)]
24. Almanza, E.; Pérez, M.J.; Rodríguez, N.A.; Murr, L.E. Corrosion resistance of Ti-6Al-4V and ASTM F75 alloys processed by electron beam melting. *J. Mater. Res. Technol.* **2017**, *6*, 251–257. [[CrossRef](#)]
25. Gong, X.; Li, Y.; Nie, Y.; Huang, Z.; Liu, F.; Huang, L.; Jiang, L.; Mei, H. Corrosion behaviour of CoCrMo alloy fabricated by electron beam melting. *Corros. Sci.* **2018**, *139*, 68–75. [[CrossRef](#)]
26. Xiang, D.D.; Wang, P.; Tan, X.P.; Chandra, S.; Wang, C.; Nai, M.; Tor, S.B.; Liu, W.Q.; Liu, E. Anisotropic microstructure and mechanical properties of additively manufactured Co–Cr–Mo alloy using selective electron beam melting for orthopedic implants. *Mater. Sci. Eng. A* **2019**, *765*, 138270. [[CrossRef](#)]
27. Bandyopadhyay, A.; Shivaram, A.; Isik, M.; Avila, J.D.; Dernell, W.S.; Bose, S. Additively manufactured calcium phosphate reinforced CoCrMo alloy: Bio-tribological and biocompatibility evaluation for load-bearing implants. *Addit. Manuf.* **2019**, *28*, 312–324. [[CrossRef](#)]
28. Koopmann, J.; Voigt, J.; Niendorf, T. Additive Manufacturing of a Steel–Ceramic Multi-Material by Selective Laser Melting. *Metall. Mater. Trans. B* **2019**, *50*, 1042–1051. [[CrossRef](#)]
29. Wen, Y.; Zhang, B.; Narayan, R.L.; Wang, P.; Song, X.; Zhao, H.; Ramamurty, U.; Qu, X. Laser powder bed fusion of compositionally graded CoCrMo-Inconel 718. *Addit. Manuf.* **2021**, *40*, 101926. [[CrossRef](#)]
30. Jung, A. Die Jagd nach dem Schatz im Autoschrott. *Spiegel* **2019**, *11*, 73.
31. Sommer, N.; Stredak, F.; Böhm, S. High-Speed Laser Cladding on Thin-Sheet-Substrates—Influence of Process Parameters on Clad Geometry and Dilution. *Coatings* **2021**, *11*, 952. [[CrossRef](#)]
32. Calleja, A.; Taberero, I.; Ealo, J.A.; Campa, F.J.; Lamikiz, A.; de Lacalle, L.N.L. Feed rate calculation algorithm for the homogeneous material deposition of blisk blades by 5-axis laser cladding. *Int. J. Adv. Manuf. Technol.* **2014**, *74*, 1219–1228. [[CrossRef](#)]
33. Deutsches Institut für Normung e. V. *Metallische Werkstoffe—Zugversuch—Teil 1: Prüfverfahren bei Raumtemperatur (ISO/FDIS 6892-1:2019): German and English Version prEN ISO 6892-1:2019*; Beuth Verlag GmbH: Berlin, Germany, 2019.
34. Sommer, N.; Kryukov, I.; Wolf, C.; Wiegand, M.; Kahlmeyer, M.; Böhm, S. On the Intergranular Corrosion Properties of Thin Ferritic Stainless Steel Sheets Welded by Fiber-Laser. *Metals* **2020**, *10*, 1088. [[CrossRef](#)]
35. David, S.A.; Vitek, J.M. Correlation between solidification parameters and weld microstructures. *Int. Mater. Rev.* **1989**, *34*, 213–245. [[CrossRef](#)]
36. Bauer, A. Hochttemperatureigenschaften Polykristalliner γ' -gehärteter Kobaltbasis-Superlegierungen. Ph.D. Thesis, Friedrich-Alexander-Universität Erlangen-Nürnberg and FAU University Press ein Imprint der Universität Erlangen-Nürnberg, Erlangen, Germany, 2015.
37. Alvarez, P.; Montealegre, M.A.; Cordovilla, F.; García-Beltrán, A.; Angulo, I.; Ocaña, J.L. Direct Generation of High-Aspect-Ratio Structures of AISI 316L by Laser-Assisted Powder Deposition. *Materials* **2020**, *13*, 5670. [[CrossRef](#)]